Supporting Information

Universal Upconversion Amplification via 4d-4f Hybridization in Ln^{3+}/MoO_4^{2-} Co-doped Fluorapatite: Mechanism and Applications

*Boyang Wang, Yuankun Ren, Xiaohan Wei, Wei Yang, Haoming Su, Yu Liu, Jiaqi Liang, Xiyu Li**

B. Wang, Y. Ren, X. Wei, W. Yang, Y. Liu, J. Liang, X. Li

State Key Laboratory of Oral Diseases & National Center for Stomatology & National Clinical Research Center for Oral Diseases, West China Hospital of Stomatology

Sichuan University

Chengdu, Sichuan, 610041, China

Email: lixiyu@scu.edu.cn (X. Li)

H. Su

Department of Chemistry

Tufts University

Medford, MA, 02155, USA

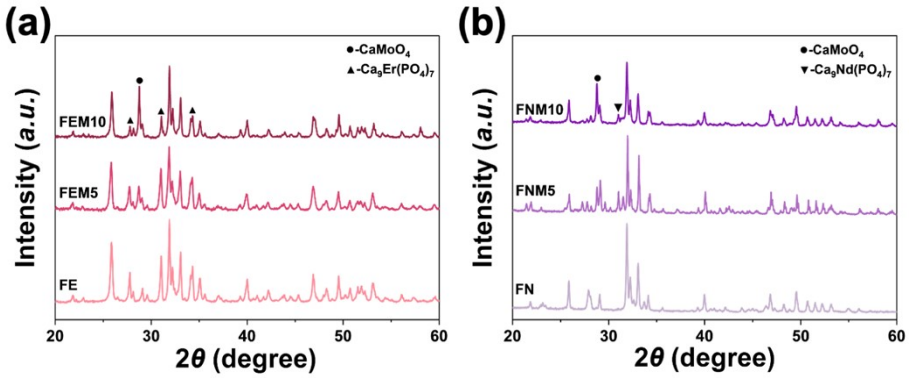

Figure S1. XRD patterns of FEM a) and FNM b) samples.

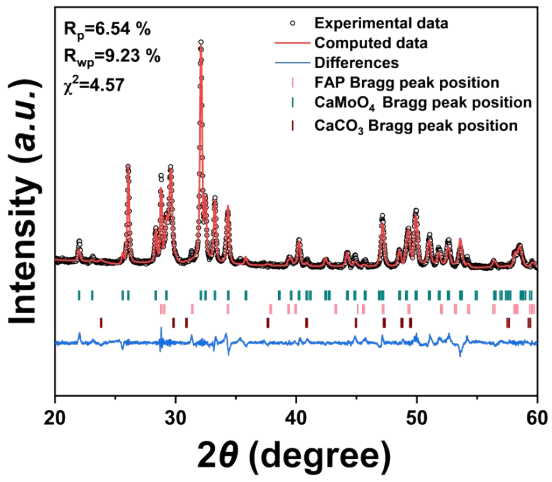

Figure S2. Rietveld refinement result of FYEM. The corresponding lattice parameters, space groups and weight percentage are concluded in Table S3.

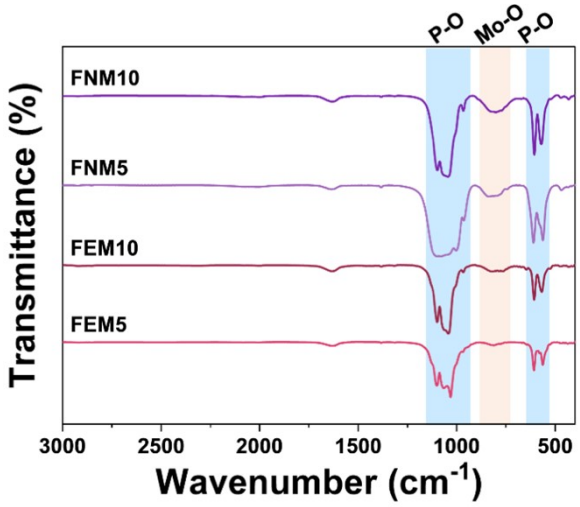

Figure S3. FTIR spectra of FEM and FNM samples.

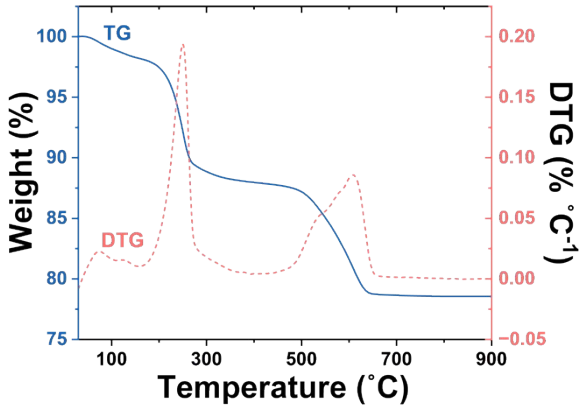

Figure S4. TG-DSC curves of FYEM heated from room temperature (30 ˚C) to 900 ˚C. Weigh loss from room temperature to 300 ˚C is attributed to water loss, and that from 500–650 ˚C is attributed to carbonate decomposition [S1]. Notably, only a slight weight loss (~0.09 wt%) occurs in the period of 700–900 ˚C, supporting its thermal stability.

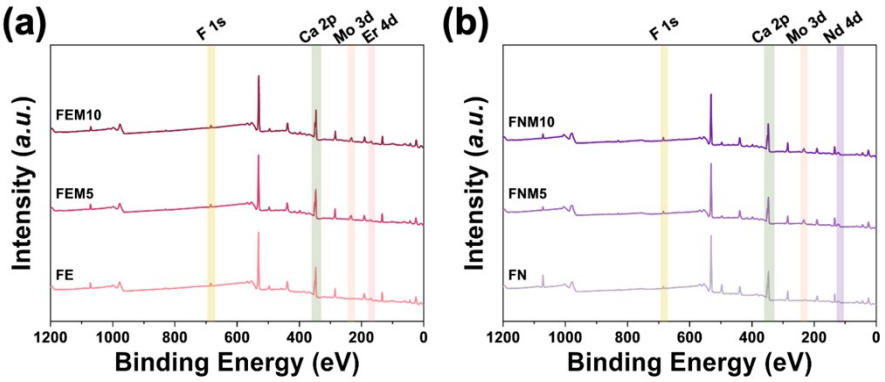

Figure S5. XPS survey spectra of FEM a) and FNM b) samples.

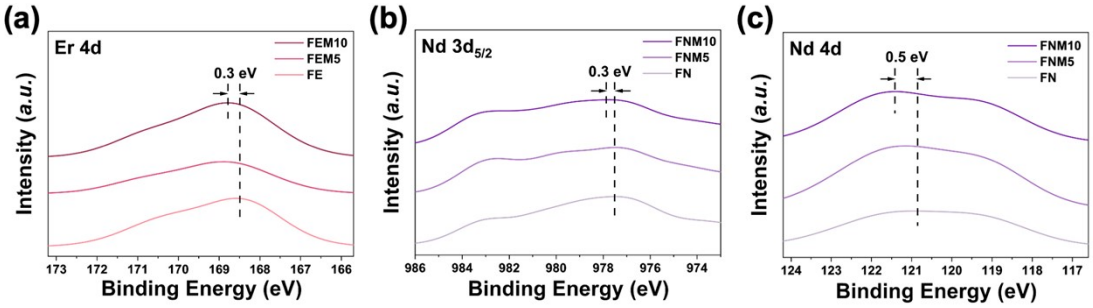

Figure S6. The Er 4d a), Nd $3d_{5/2}$ b), and Nd 4d c) XPS high-resolution spectra of FEM and FNM samples.

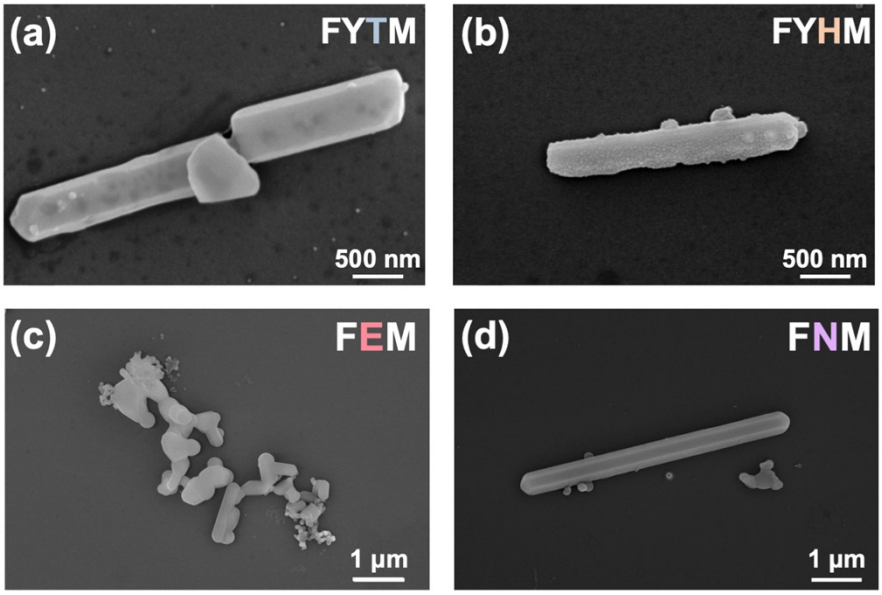

Figure S7. SEM images of FYTM a), FYHM b), FEM c), and FNM d).

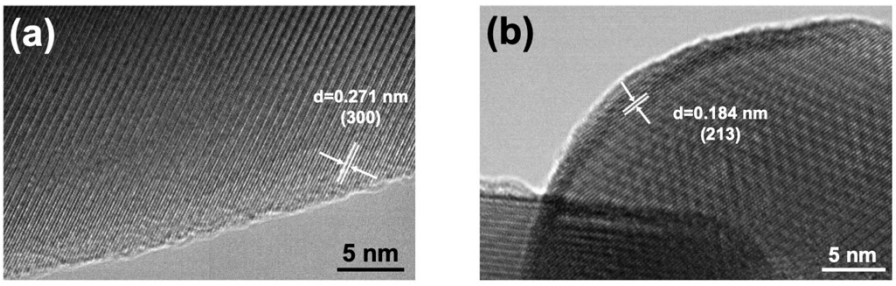

Figure S8. HRTEM images of FYEM obtained at the edge of a rod a) and a spherical particle b). Both exhibit crystal plane of FAp.

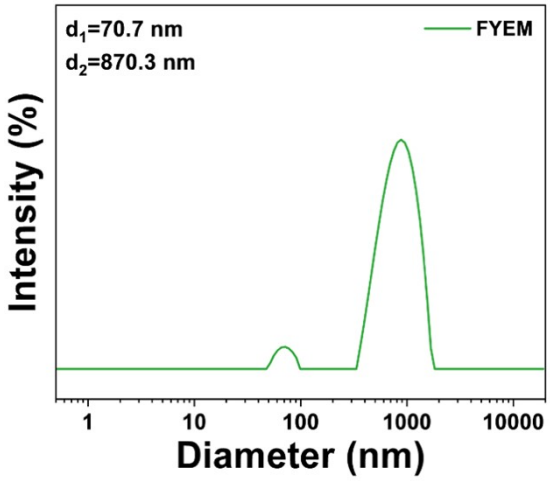

Figure S9. Hydrodynamic diameter of FYEM after sintering.

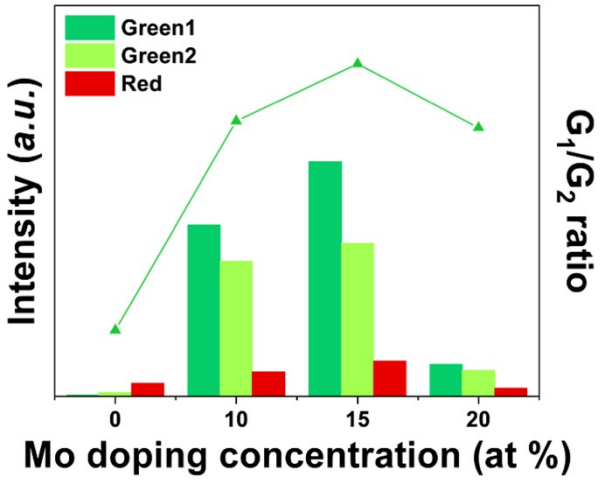

Figure S10. Integrated upconversion luminescence and the ratio of G_1/G_2 of FYEM.

The two components of green emission of Er^{3+} derive from $^2H_{11/2}$–$^4I_{15/2}$ (G_1) and $^4S_{3/2}$–$^4I_{15/2}$ (G_2). The two energy levels, $^2H_{11/2}$ and $^4S_{3/2}$ are thermally coupled under room temperature. Interestingly, we discovered that doping MoO_4^{2-} favors emission from $^2H_{11/2}$, as indicated by G_1/G_2 ratio in Figure S8. We assume that this prevalence is probably caused by a better matching between $^2H_{11/2}$ and $|^2F_{7/2}$, $^3T_2>$.

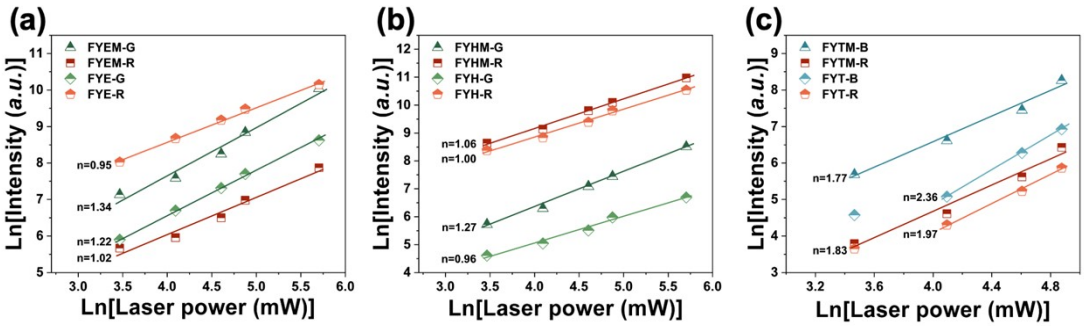

Figure S11. Power-dependent log-log plot of UCL of FYXM samples under 980 nm excitation. G/B/R represents green, blue and red emissions respectively. The peak intensity of each emission was used to calculate log-log plot.

The pumping process of Tm^{3+} is much easier than that of Er^{3+} and Ho^{3+}. Therefore, the alteration in decay lifetime (Figure 2i) and *n* value (Figure S11c) is discussed in main text. Er^{3+} and Ho^{3+} are acknowledged to absorb phonon at a wavelength of 980 nm. On the other hand, they own more energy levels and their pumping process thus involve complicated GSA/ESA and CR processes. In Figure 2g, it is observed that rise time lengthens for $^2H_{11/2}$ of Er^{3+}, in parallel with the elevated *n* value in Figure S9a. The reason lies in the GSA and ESA process of Er^{3+} itself. Although at a relatively low concentration, Er^{3+} in FYEM could be excited by 980 nm excitation and cooperate with ET process to emit green and red UCL. This could be deduced from the relatively sharp

rise edge and a fast rise time (54 μs and 65 μs) for both green and red emissions (Table S6). After doping MoO_4^{2-}, HESET with much efficiency takes place and contributes more to the pumping process. This results in elevated slope, prolonged rise time as observed in Figure 2g and Figure S9a.

Similarly, the pumping process of Ho^{3+} involves ESA as well. In parallel with recent research conducted by Wei et al. [S2], the rise edge for green emission for green emission is much sharper than that of red emission, exhibiting a rise time of 40 μs (Figure 2h). Here the effect of contribution of HESET is more pronounced (from 40 μs to 104 μs), because of the lower concentration of Ho^{3+}.

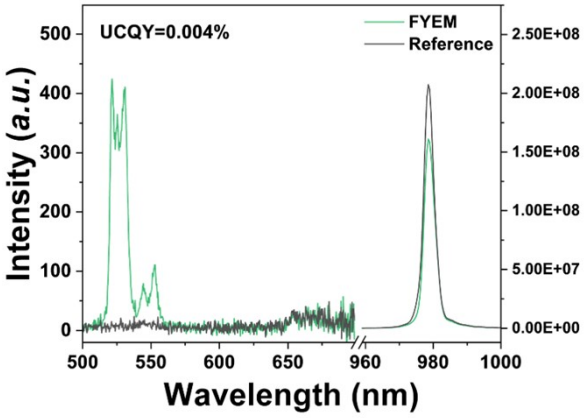

Figure S12. Upconversion quantum yield examination of FYEM.

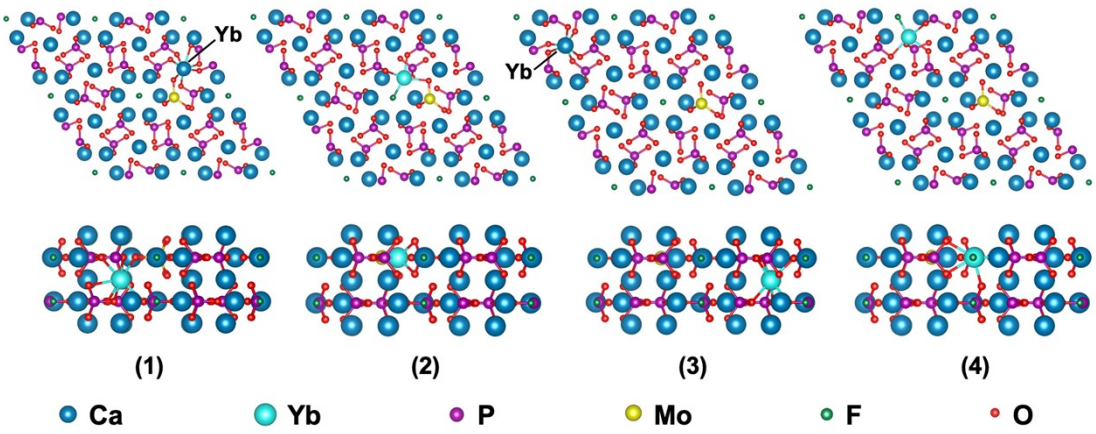

Figure S13. Crystal cell models of Yb/Mo co-doped fluorapatite with superior view and lateral view. 1). Yb replaces Mo-adjacent Ca1 site. 2). Yb replaces Mo-adjacent Ca2 site. 3). Yb replaces Mo-distant Ca1 site. 4). Yb replaces Mo-distant Ca2 site.

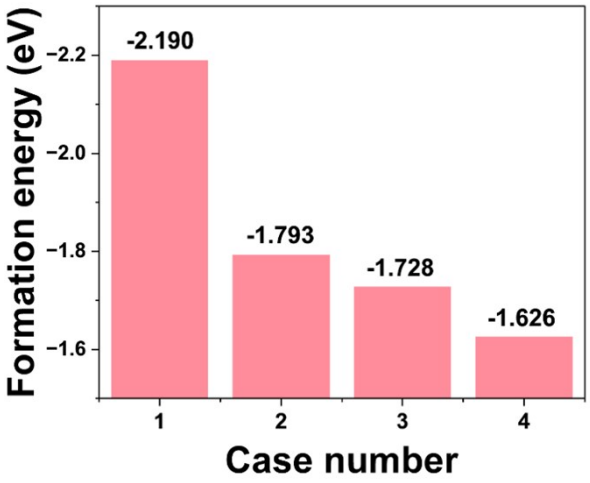

Figure S14. DFT calculated formation energy of different cases of Yb and/or Mo substitutions in FAp crystal cell.

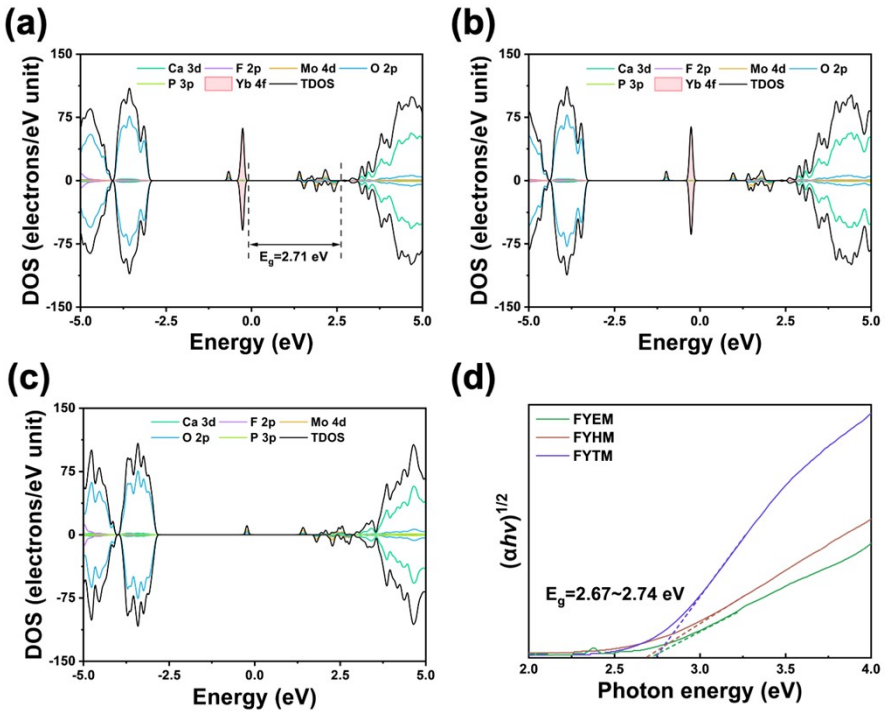

Figure S15. TDOS and PDOS of case 2 a), case 3 b), and Yb-undoped case c) calculated by DFT. The contribution of Yb 4f is filled to draw a distinction. d). Tauc plot of FYXM samples.

As shown in Figure S15a, the bandgap of Yb^{3+}/MoO_4^{2-} co-doped fluorapatite is around 2.71 eV. Given that the transition from ground state of MoO_4^{2-} to triplet excited state is spin forbidden, the TDOS from ~1 eV to 2.5 eV which is dominantly contributed by MoO_4^{2-} is omitted while considering bandgap.

The optical bandgap energy of FYXM samples is calculated by tauc plot from absorption edges from the following equation:

$$(\alpha hv)^{\gamma} = A(hv - E_g) \quad \text{(S1)}$$

where γ is accepted to be 1/2 because of the assumed indirectly allowed transition. The optical bandgap is calculated to be 2.67–2.74 eV for all FYXM samples (Figure S15d), consistent with the result obtained in DFT. This consistency indicated an appropriate selection of effective U value.

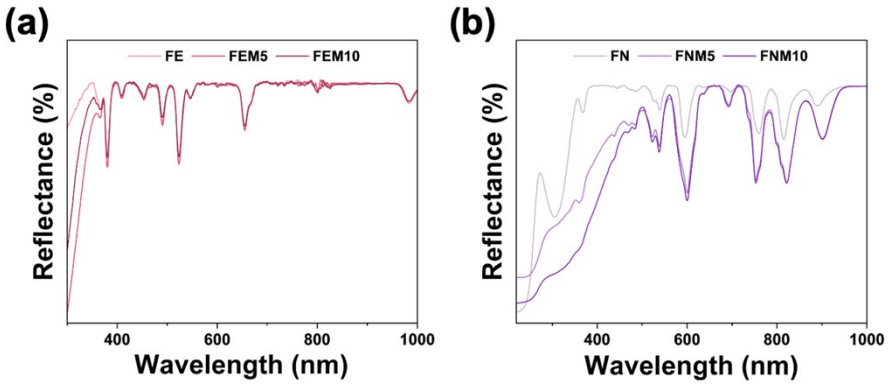

Figure S16. UV-Vis-NIR reflectance spectra of FEM a) and FNM b) samples.

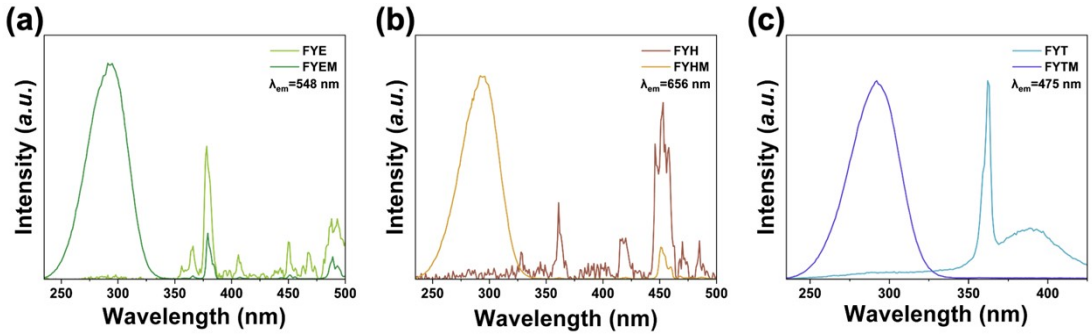

Figure S17. Excitation spectra of FYXM samples. The emission wavelength is chosen by their respective characteristic emission.

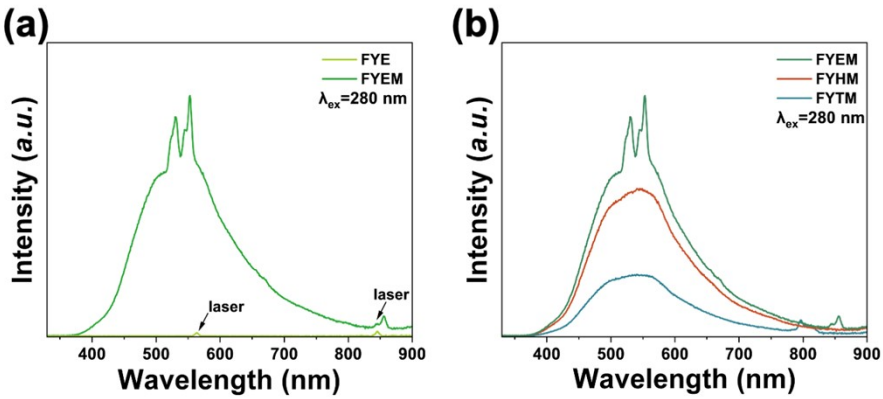

Figure S18. a). Downconversion luminescence (DCL) spectra of FYE and FYEM under 280 nm excitation; b) DCL spectra of FYXM under 280 nm excitation.

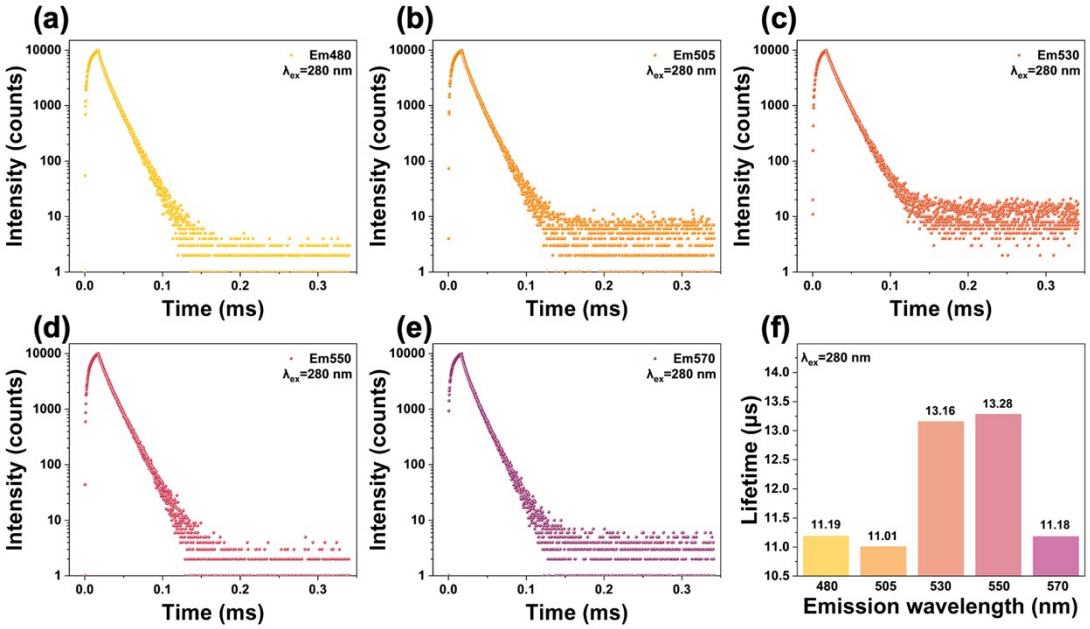

Figure S19. a-e). Downconversion decay time of FYEM under 280 nm excitation. f). Comparison of decay lifetime at different wavelength.

The decay lifetime is recorded at different wavelength selected from Figure S16b. Remarkably, the lifetime is prolonged for emissions at 530 nm and 550 nm, where Er^{3+} exhibits additional characteristic emissions. The energy transfer process occurs from MoO_4^{2-} towards Er^{3+} and both contribute to the decay, thereby lengthening lifetime at about 20%. The lifetime at 480 nm is similar to that at 570 nm demonstrating that their emission may share a same decay pathway, probably the intrinsic decay in MoO_4^{2-}.

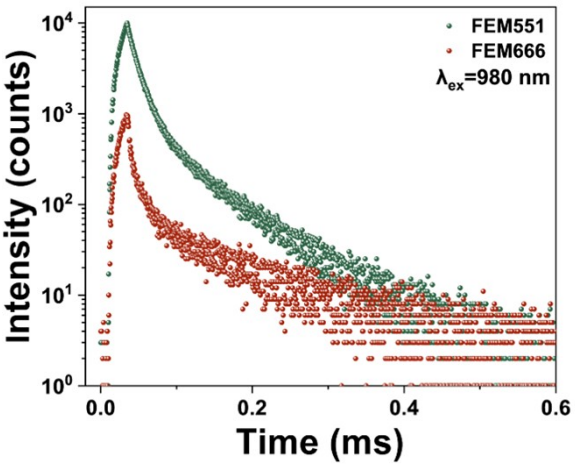

Figure S20. Upconversion luminescence decay time of FEM5 under 980 nm excitation.

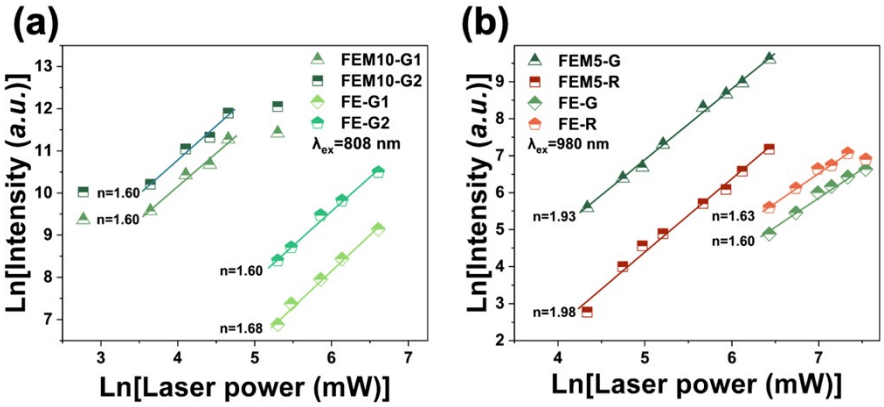

Figure S21. Upconversion luminescence log-log plot of FE and FEM under 808 nm excitation a) and 980 nm excitation b).

The rise time of FEM5 under 980 nm excitation is significantly shorter than that of FYEM (Figure S20, Table S8). When excited by 980 nm, a typical SSU process requires a successive ESA after electrons being pumped to $^4I_{11/2}$ via ground state absorption (GSA). However, electrons on $^4I_{11/2}$ are liable to relax towards $^4I_{13/2}$ via MPR, which could account for the extremely weak UCL of FE under 980 nm excitation. The formation of Er^{3+}/MoO_4^{2-} dimer could supply much more energy levels for electrons to

relax onto, thus rendering more probability for electrons to get pumped into high-energy levels via GSA, ESA and possible relaxation. Moreover, the elevation of *n* value is indicative of an energy transfer process from Er^{3+}/MoO_4^{2-} to Er^{3+} (Figure S21b).

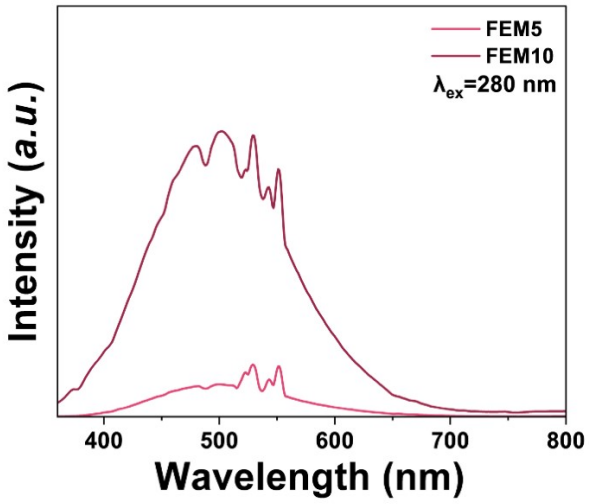

Figure S22. Downconversion luminescence spectra of FEM under 280 nm excitation.

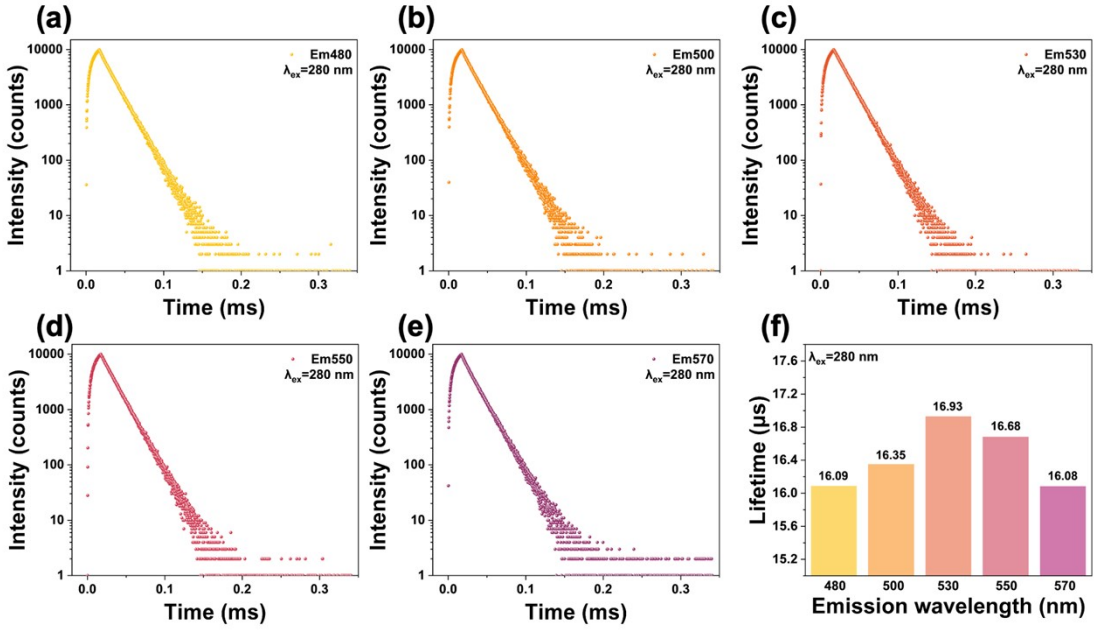

Figure S23. a-e). Downconversion decay time of FEM10 under 280 nm excitation. f). Comparison of decay lifetime at different wavelength.

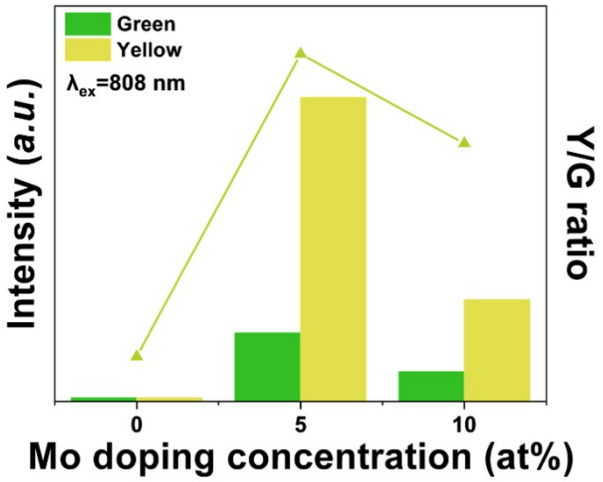

Figure S24. Relative intensity of yellow and green UCL (bar) and Y/G ratio (dotted line) of FNM.

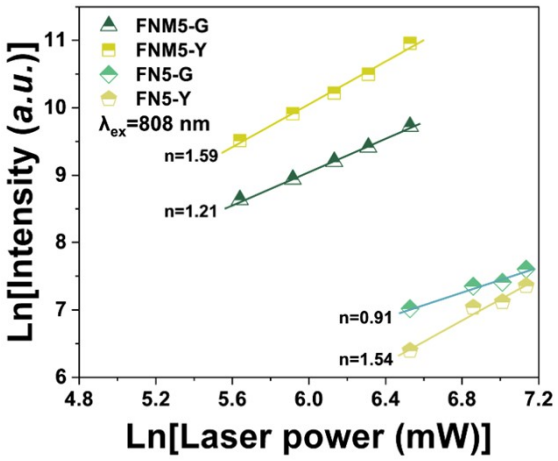

Figure S25. Upconversion luminescence power-dependent log-log plot of FN and FNM under 808 nm excitation.

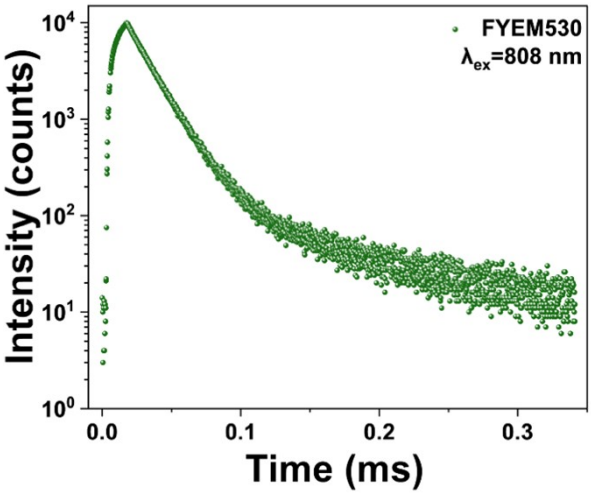

Figure S26. Upconversion luminescence decay time of emission at 530 nm of FYEM under 808 nm excitation.

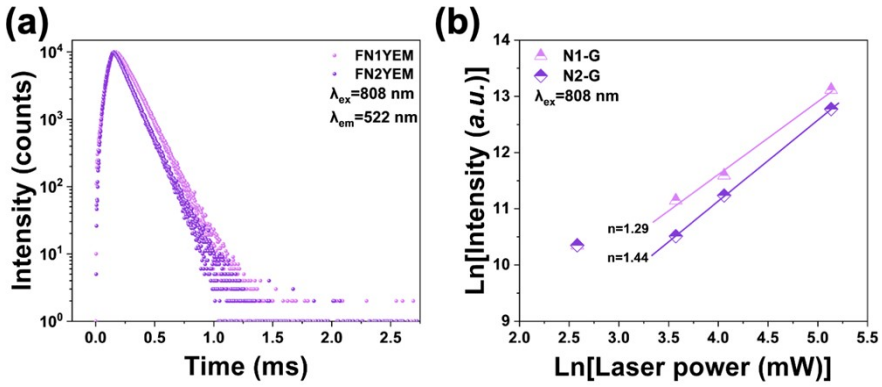

Figure S27. Upconversion luminescence decay time a), log-log plot of FNYEM under 808 nm excitation b).

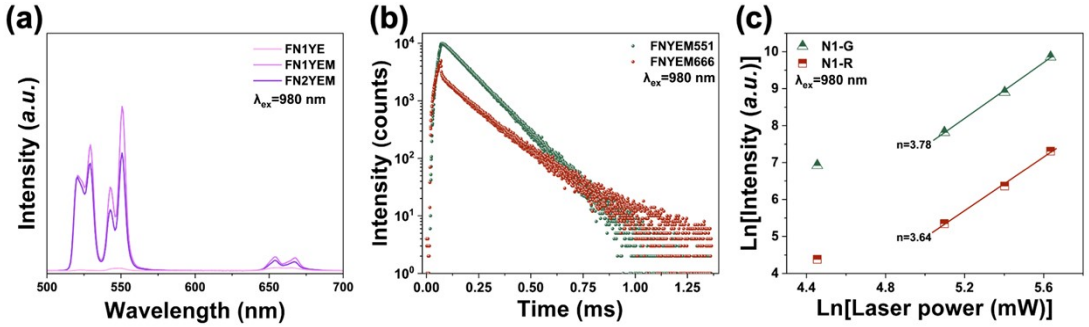

Figure S28. Upconversion luminescence spectra a), decay time b), log-log plot of FNYEM under 980 nm excitation c).

The intensity of UCL decrease as the Nd^{3+} increases from 1% to 2% (Figure S28a), indicating the incorporation of Nd^{3+} interferes the upconversion process of Yb^{3+}/Er^{3+}. This phenomenon is evident in that FNYE did not show UCL under 808 nm excitation (Figure 5b), while FYE exhibits weak yet observable UCL in Figure 5a. Another evidence lies in the elevated *n* value in Figure S28c. The mechanism might be the cross relaxation between Nd^{3+} and Er^{3+}, hindering the pumping process towards higher energy levels of Er^{3+}.

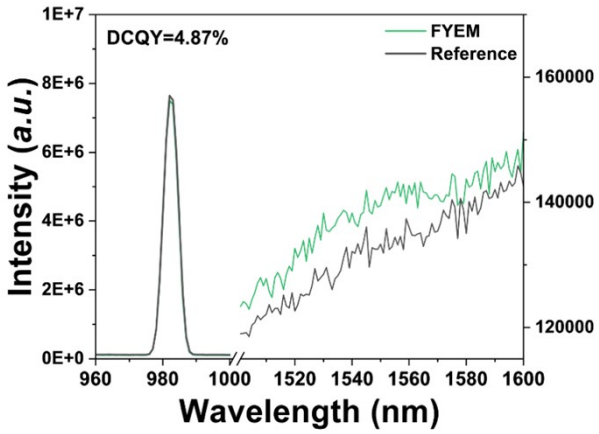

Figure S29. Downconversion quantum yield of FYEM sample under 980 nm excitation.

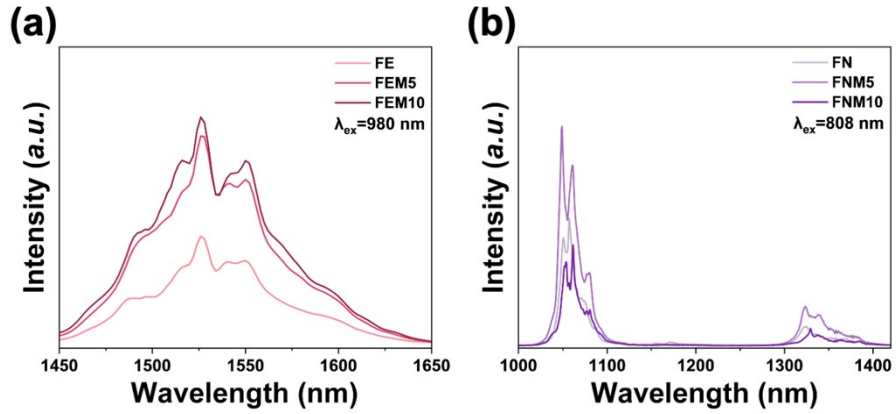

Figure S30. Downconversion luminescence spectra of FEM a) and FNM b) in the region of NIR-II.

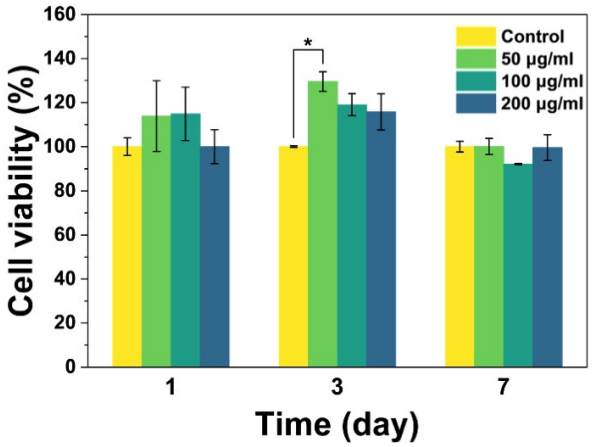

Figure S31. Cytocompatibility assay of FYEM sample at various concentrations.

Table S1. Dopant molar concentration of FYX (FAp:Yb/X) and FYXM (FAp:Yb/X/Mo) samples at synthesis.

Sample	Ca mol%	Yb mol%	X (Er/Ho/Tm) mol%	PO_4^{3-} mol%	MoO_4^{2-} mol%	(Ca+Ln)/ (P+Mo)
FYE	89.5	10	0.5	60	-	1.67
FYEM	89.5	10	0.5	51	9	1.67
FYH	89.9	10	0.1	60	-	1.67
FYHM	89.9	10	0.1	54	6	1.67
FYT	79.9	20	0.1	60	-	1.67
FYTM	79.9	20	0.1	55.2	4.8	1.67

Table S2. Dopant molar concentration of FEM (FAp:Er/Mo), FNM (FAp:Nd/Mo), and FNYEM (FAp:Nd/Yb/Er/Mo) samples at synthesis.

Sample	Ca mol%	Yb mol%	Er mol%	Nd mol%	PO_4^{3-} mol%	MoO_4^{2-} mol%	(Ca+Ln)/ (P+Mo)
FE	95	-	5	-	60	-	1.67
FEM5	95	-	5	-	57	3	1.67
FEM10	95	-	5	-	54	6	1.67
FN	95	-	-	5	60	-	1.67
FNM5	95	-	-	5	57	3	1.67
FNM10	95	-	-	5	54	6	1.67
FN1YE	88.5	10	0.5	1	60	-	1.67
FN1YEM	88.5	10	0.5	1	51	9	1.67
FN2YEM	87.5	10	0.5	2	51	9	1.67

Table S3. Rietveld refinement results of FYEM

Phase	Space group	Lattice parameters						Weight percentage (wt%)
		a (Å)	b (Å)	c(Å)	α(°)	β(°)	γ(°)	
Fluorapatite	*P63/m*	9.33467	9.33467	6.83695	90	90	120	93.9
$CaMoO_4$	*I41/a*	5.22578	5.22578	11.40638	90	90	90	0.8
$CaCO_3$	*R-3c*	4.77962	4.77962	17.36788	90	90	120	5.3

Table S4. Observed major vibrational frequencies (cm^{-1}) FYX and FYXM samples and corresponding assignments [S3, S4]. Asterisk (*) denotes indistinguishable peak.

Assignments	FYE	FYEM	FYH	FYHM	FYT	FYTM
$v_4(PO_4)$	606	609	608	608	607	608
$v_1(PO_4)$	963	963	964	962	963	962
$v_3(PO_4)$	1099	1099	1099	1100	-*	-*
$v_4(MoO_4)$	-	563	-	562	-	560
$v_3(MoO_4)$	-	834	-	836	-	841
$v_1(MoO_4)$	-	1001	-	999	-	998
$v_3(CO_3)$	1421	1418	1418	1422	1420	1419

Table S5. Comparison of doped and tested dopant molar concentration obtained by ICP-MS analysis in FYX and FYXM samples.

Group	Yb:Ln mol%		Mo:P mol%		(Ca+Ln)/ (P+Mo)
	Doped	Tested	Doped	Tested	Tested
FYE	10:0.5	11.35:0.57	-		1.53
FYEM	10:0.5	11.23:0.59	15	15.35	1.53
FYH	10:0.1	11.35:0.10	-		1.52
FYHM	10:0.1	10.65:0.10	10	8.96	1.50
FYT	20:0.1	20.32:0.11	-		1.47
FYTM	20:0.1	19.35:0.10	8	6.7	1.53

Table S6. Rise and decay times of FYXM samples under 980 nm excitation.

Group	Rise time (μs)		Decay time (μs)	
	522 nm	654 nm	522 nm	654 nm
FYE	54	84	52	402
FYEM	65	94	129	297
	540 nm	650 nm	540 nm	650 nm
FYH	40	213	118	379
FYHM	107	196	137	332
	475 nm	648 nm	475 nm	648 nm
FYT	181	180	217	227
FYTM	152	149	143	216

Table S7. Rise time of samples under 808 nm excitation.

Group	Rise time (μs)		Decay time (μs)	
	530 nm	550 nm	530 nm	550 nm
FN1YEM	118	116	121	120
FN2YEM	112	113	111	110
FE5	4.42	4.42	0.34	0.36
FE5M10	7.25	6.50	14.7	13.5
FYEM	10.1	9.92	18.0	18.1
	532 nm	595 nm	532 nm	595 nm
FN5	90.7	78	66.2	69.1
FN5M5	46	48.3	30.6	30.0

Table S8. Rise time of samples under 980 nm excitation.

Group	Rise time (μs)		Decay time (μs)	
	551 nm	666 nm	551 nm	666 nm
FN1YEM	60	51.7	105	77.5
FE5	undetectable			
FE5M10	27.5	26.7	17.1	13.5
FYEM	62.7	89.3	129	297

References

[S1] Senra, M. R., de Lima, R. B., Souza, D. d. H. S., Marques, M. d. F. V., Monteiro, S. N., Thermal characterization of hydroxyapatite or carbonated hydroxyapatite hybrid composites with distinguished collagens for bone graft, *Journal of Materials Research and Technology*, 2020, 9, 7190-7200.

[S2] Wei H.; Cai Z.; Wei G.; Zhou B. Ultra-Sensitive Low-Temperature Upconversion via Interfacial Energy Transfer Toward Visual Cryogenic Nanothermometry. *Advanced Functional Materials*, 2025, e10764.

[S3] Panda, R., Hsieh, M., Chung, R., Chin, T., FTIR, XRD, SEM and solid state NMR investigations of carbonate-containing hydroxyapatite nano-particles synthesized by hydroxide-gel technique, *Journal of Physics and Chemistry of Solids*, 2003, 64, 193-199.

[S4] Zouaoui, M., Jendoubi, I., Zid, M. F., Bourguiba, N. F., Synthesis, crystal structure and physico-chemical investigations of a new lyonsite molybdate $Na_{0.24}Ti_{1.44}(MoO_4)_3$, *Journal of Solid State Chemistry*, 2021, 300, 122221.